

Adaptive Array of Phase-Locked Fiber Collimators: Analysis and Experimental Demonstration

Mikhail A. Vorontsov, Thomas Weyrauch, Leonid A. Beresnev, Gary W. Carhart, Ling Liu, and Konley Aschenbach

(Invited Paper)

Abstract—We discuss development and integration of a coherent fiber array system composed of densely packed fiber collimators with built-in capabilities for adaptive wavefront phase piston and tilt control at each fiber collimator. In this system, multi-channel fiber-integrated phase shifters are used for phase locking of seven fiber collimators and the precompensation of laboratory-generated turbulence-induced phase aberrations. Controllable x and y displacements of the fiber tips in the fiber collimator array provide additional adaptive compensation of the tip and tilt phase aberration components. An additional control system is utilized for equalization of the intensity of each of the fiber collimator beams. All three control systems are based on the stochastic parallel gradient descent optimization technique. The paper presents the first experimental results of adaptive dynamic phase distortion compensation with an adaptive phase-locked fiber collimator array system.

Index Terms—Adaptive optics (AO), optical arrays, optical beams, phased arrays.

I. INTRODUCTION

IN RECENT years, we have witnessed increasing demand for laser transmitter systems (commonly referred to also as laser beam-forming telescopes and beam directors) for various atmospheric optics applications including active imaging, remote spectroscopy, beam projection on a remote target, free-space laser communications, laser target tracking and interrogation, etc. At present, laser transmitter systems operate in the atmosphere over a wide range of propagation distances from several meters up to hundreds of kilometers and correspondingly require beam-forming telescopes of different aperture sizes (from a few centimeters in diameter for short-range use up to 1 m or even larger for space applications). Medium- and large-aperture telescopes are commonly equipped with quite sophisticated and expensive servo-systems for outgoing laser beam pointing. It is quite apparent that development of such systems consumes

Manuscript received October 15, 2008; revised December 1, 2008. First published January 27, 2009; current version published April 8, 2009. This work was supported in part by the Defense Advanced Research Projects Agency (DARPA) and the Joint Technology Office and by the Cooperative Agreements between Army Research Laboratory (ARL) and the University of Maryland, College Park, under Contracts W911NF-06-2-0009 and W911NF-07-2-0009.

M. A. Vorontsov is with the Computational and Information Sciences Directorate, U.S. Army Research Laboratory, Adelphi, MD 20783 USA, and also with the Institute for Systems Research, University of Maryland, College Park, MD 20742 USA (e-mail: mvorontsov@arl.army.mil).

T. Weyrauch and L. Liu are with the Institute for Systems Research, University of Maryland, College Park, MD 20742 USA (e-mail: weyrauch@umd.edu; liuling@umd.edu).

L. A. Beresnev, G. W. Carhart, and K. Aschenbach are with the Computational and Information Sciences Directorate, U.S. Army Research Laboratory, Adelphi, MD 20783 USA (e-mail: lberesnev@arl.army.mil; gcarhart@arl.army.mil; konley.aschenbach@arl.army.mil).

Digital Object Identifier 10.1109/JSTQE.2008.2010875

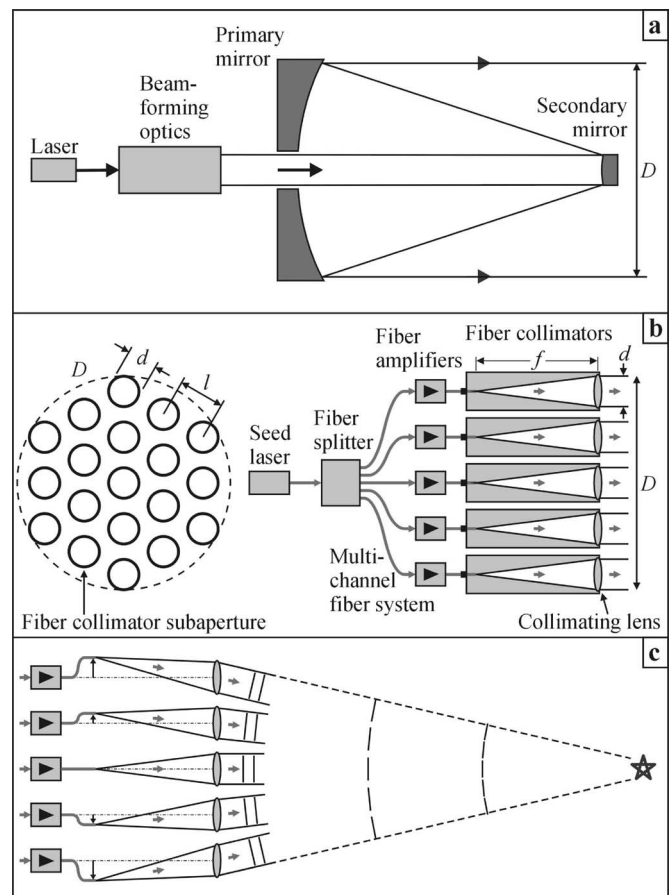


Fig. 1. Laser transmitter system configurations based on (a) a conventional telescope system and (b) an array of fiber amplifiers and phase-locked fiber collimators with a focal length f , a diameter d , and a center-to-center distance l . Notional schematic (c) illustrates beam focusing in a fiber array performed by fiber tip displacements to appropriate off-axis positions.

significant time and resources, the requirements of which are growing nearly exponentially with the increase of the beam director aperture size (diameter D).

In this paper, we consider a recently emerging modular approach for development of laser transmitter systems [1]–[7]. In this approach, a conventional beam-forming telescope with monolithic optics [commonly the primary and secondary mirrors as illustrated in Fig. 1(a)] is replaced by an array of smaller size fiber collimators shown in Fig. 1(b).

For definiteness, we consider here a beam director in the form of a hexagonal array of lens-based fiber collimators with circular apertures (subapertures) of diameter d and the distance

between the centers of neighboring subapertures l . The system aperture diameter can be defined in this case by a circle of the smallest diameter D that contains all N_{sub} subapertures of the fiber array, as illustrated in Fig. 1(b) (picture at the left). Note that the increase of the fiber array overall aperture size D does not change the system width h , which now depends on the focal length f of the collimating lens in the fiber collimator and can be roughly approximated by $h \approx f$. Assuming that $f \approx 6d$, which is a typical requirement for manufacturing high-quality lenses, and $d \ll D$ (fiber array with a large number N_{sub} of subapertures), the system width h can be significantly smaller than the aperture diameter: $h \approx 6d \ll D$. For this reason, the fiber collimator array system is also often referred to as a *conformal beam-forming system* or *conformal aperture* for short [5], [7].

To minimize the outgoing beam divergence, the beams emitted by the fiber collimators (beamlets) should be locked in phase. In this study, we consider only phase-locked fiber collimator array systems, also known as phased fiber arrays [5], [6].

Conformal beam-forming systems have several advantages over conventional beam directors with monolithic mirrors.

First, conformal laser transmitters of various aperture sizes can be assembled using identical building blocks—fiber collimators. This eliminates the need for redesigning and manufacturing unique beam-forming telescopes for each specific application.

Second, being composed of relatively small-size fiber collimators, a large-aperture conformal beam director system can be significantly lighter than the equivalent conventional laser transmitter based on monolithic optical elements. Consequently, the fiber collimator array system can be integrated on a lighter and more precise gimbal for beam pointing and target tracking.

Third, in conventional beam-forming telescopes, outgoing beam focusing (projection) is performed using mechanical displacement of an optical element (commonly the telescope's secondary mirror) along the optical axis. This results in relatively slow (from hundreds of milliseconds up to several seconds, depending on telescope size) transmitter system refocusing. In fiber array systems, outgoing beam refocusing can be performed by tilting wavefront phase of the outgoing beamlets at the fiber collimator system pupil, as shown in Fig. 1(c). This phase tilt control at each fiber collimator subaperture can be implemented significantly faster (at a millisecond time scale), for example, by displacing a fiber tip as illustrated in Fig. 1(c) and discussed in Section II. Fast control of the beamlet phase tilts can also be used for active mitigation of the outgoing beam jitter resulting from mechanical vibrations—a common problem with conventional beam directors.

Fourth, beam director architecture based on a phased array of fiber collimators is robust to element failure, which is especially important for system operation in hazardous environments.

Finally, in fiber array laser transmitter systems, atmospheric turbulence-induced phase distortions can be precompensated using adaptive optics (AO) elements (wavefront correctors with sensing and control systems) that are directly integrated into fiber collimators. In this AO system architecture, wavefront phase control functions are distributed between subapertures and for this reason can be referred to as distributed AO (DAO) [8]. In the DAO system described in Section III, the fiber-integrated

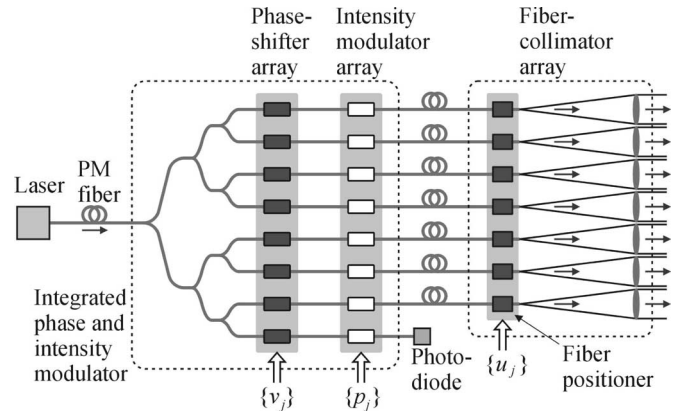


Fig. 2. Notional schematic of the fiber-array-based laser beam transmitter system.

phase shifters are used not only for locking of phases between beamlets but also for compensation of the turbulence-induced piston-type (subaperture averaged) phase aberration components. Since these phase shifters can be extremely fast, the piston-type phase aberrations can be compensated using an AO control system with more than 100 kHz closed-loop bandwidth. Such compensation bandwidth cannot be achieved with conventional AO elements (deformable mirrors).

The paper is organized as follows. In Section II, we discuss different issues related with the development, integration, and experimental demonstration of a phase-locked fiber array system with built-in capabilities for adaptive wavefront phase piston and tilt control at each fiber collimator. Adaptive feedback control systems used for phase-locking, wavefront phase tip and tilt control, and power equalization are described in Section III. The experiments with adaptive precompensation of dynamic phase aberrations are discussed in Section IV.

II. DEVELOPMENT OF FIBER COLLIMATOR ARRAY

A. Multichannel Fiber System

The notional schematic of the fiber-array-based laser beam transmitter described here is shown in Fig. 2. The fiber array consists of seven fiber collimators and a multichannel fiber system based on polarization-maintaining (PM) single-mode fiber elements. The input coherent optical beam is generated using a seed laser with $\lambda = 1.06 \mu\text{m}$ wavelength, output power up to $P_0 = 150 \text{ mW}$, and line width $\Delta f = 30 \text{ MHz}$. The laser beam is coupled to a single-mode PM fiber with a mode field diameter of $d_{\text{MFD}} = 6.6 \mu\text{m}$ and is sent into an eight-channel phase and intensity modulator. In this fully integrated solid-state device from EO SPACE, Inc. [9], the input beam is divided into eight beams with nearly equal power. Each of the eight beams sequentially propagates through an LiNbO_3 -based phase shifter and intensity (power) modulator. The intensity modulators are implemented as fiber-integrated Mach-Zehnder interferometers. The phase shifts and intensity attenuation coefficients in each channel can be changed by applying control voltages $\{v_j(t)\}$ and $\{p_j(t)\}$ on the phase shifter and intensity modulator electrodes ($j = 1, \dots, 7$). In the fiber system described, the phase shifters are used for both phase-locking of outgoing beamlets

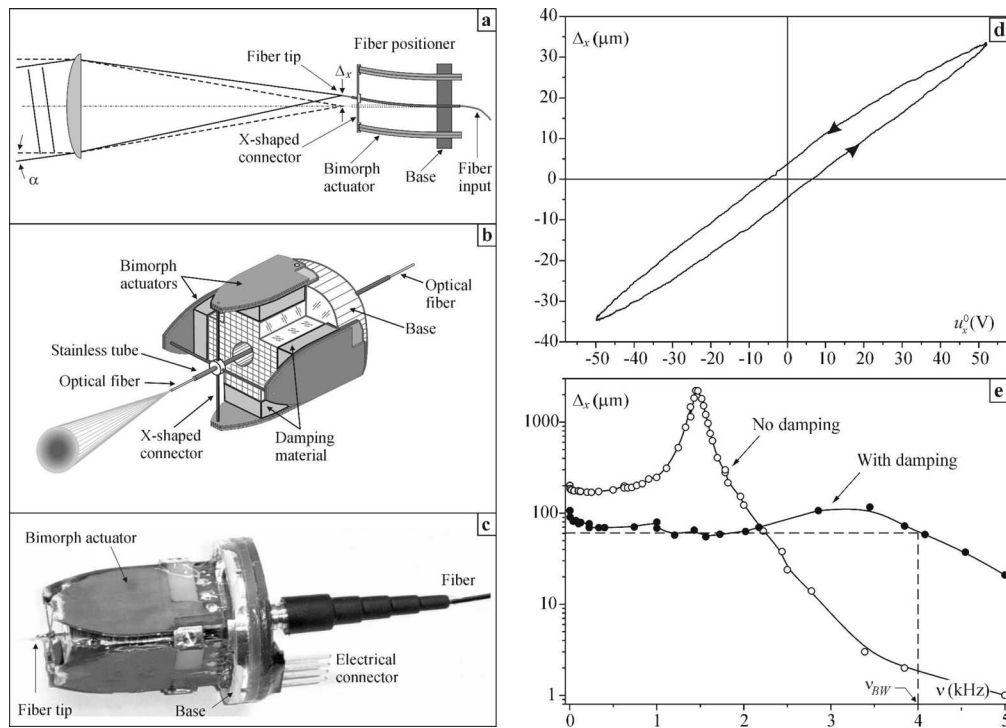


Fig. 3. Wavefront phase tip and tilt control in a fiber collimator using the fiber positioner device based on piezoelectric bimorph actuators. (a) Tip and tilt wavefront phase control using fiber tip displacement performed by a fiber positioner, (b) fiber positioner operation principal schematic, and (c) the fiber positioner assembly. (d) Fiber tip displacement amplitude Δ_x resulting from an applied harmonic signal with fixed frequency $\nu = 0.2$ Hz and (e) with fixed amplitude $u_x^0 = 70$ V with and without damping.

and compensation of piston-type phase aberrations while control of the intensity modulators is applied for equalization of the beamlet powers at the fiber collimator subapertures.

Using approximately 1.5-m-long fiber patchcords, the seven optical output ports of the phase and intensity modulator are connected with the fiber collimators. The eighth output port is fiber coupled with a photodetector and used for power level monitoring, as shown in Fig. 2. The end of each fiber entering the fiber collimator (fiber tip) is precisely positioned within a small vicinity of the collimating lens focus. Ideally (in the absence of misalignments), the fiber tip position coincides with the collimating lens focus, and thus results in a collimated outgoing beamlet exiting the lens.

B. Wavefront Tip and Tilt Control at Fiber Collimators

Wavefront phase tip and tilt control of the outgoing beamlets is performed using small x and y displacements of the fiber tip position in the focal plane of the collimating lens, as illustrated in Fig. 3(a). This fiber tip displacement is implemented using a specially designed optomechanical device referred to here as a fiber positioner [10]–[12].

The laser beam is delivered to a fiber positioner using a fiber that is fixed inside a metal tube, as shown in Fig. 3(b). The end of the metal tube with the fiber tip is fixed inside the central hole of a lightweight X-shaped connector. The four wings of this connector are attached to bimorph piezoelements (bimorph actuators).

The voltages applied to the parallel-positioned piezoelements cause the elements to bend, resulting in movement of the metal tube, and hence, fiber tip displacements Δ_x and Δ_y occurring in two orthogonal directions. In turn, the fiber tip displacement results in the corresponding beamlet phase tilt, as shown in Fig. 3(a). A photograph of a fiber positioner used in the fiber array system described here is shown in Fig. 3(c).

A typical dependence of the fiber tip displacement amplitude Δ_x on the applied voltage u_x^0 (sensitivity curve) is shown in Fig. 3(d). In the control voltage range ± 50 V, the amplitude of the fiber tip displacement $\Delta = (\Delta_x^2 + \Delta_y^2)^{1/2}$ is approximately ± 30 μm . Note that the sensitivity curve exhibits hysteresis.

The displacement Δ_x depends not only on the applied voltage amplitude u_x^0 but also on its frequency ν . The characteristic dependences of the fiber tip displacement Δ_x on the frequency ν of the sine voltage $u_x(t) = u_x^0 \sin(\nu t)$ —the fiber positioner transfer function—are shown in Fig. 3(e) in logarithmic scale. The relatively flat segment of the transfer function $0 \leq \nu \leq \nu_{BW}$ that exhibits less than 3 dB change in amplitude Δ defines the fiber positioner's operational bandwidth. The bandwidth frequency $\nu_{BW} \approx 4.0$ kHz for the fiber positioner in Fig. 3(c) was achieved by means of special passive suppression (damping) of mechanical resonances [10], [11]. Note that in absence of damping, the bandwidth frequency ν_{BW} was in the range of 500–800 Hz [compare the transfer functions of the fiber positioner with and without damping in Fig. 3(e)].

The deviation angle α of the beamlet propagation direction (wavefront tilt angle) resulting from the fiber tip displacement

is given by the following simple formula: $\alpha = \Delta/f$. Assuming that $f/d = 6$, for the deviation angle we obtain $\alpha = \Delta/(6d)$. Thus, for the fixed amplitude of the fiber positioner displacement Δ , the dynamical range of phase tilt control is inversely proportional to the subaperture diameter d . From this viewpoint, the increase of the number of fiber collimators N_{sub} (subapertures) and the corresponding decrease of d (assuming that the conformal aperture diameter D is fixed) have obvious advantage as it results in larger dynamical range of phase tip and tilt control that is available for compensation of jitter and turbulence-induced phase tilt aberrations. Besides this, the increase of angle α increases the conformal beam focusing range, as discussed in Section II-E.

In practice, there are some limitations on the fiber collimator aperture decrease since the diameter of the fiber positioner cannot be easily reduced without deterioration of its characteristics (fiber tip displacement range and operational frequency bandwidth). In addition, precise alignment of the fiber positioner itself requires some extra space between the fiber positioner holders so that the distance between the centers of neighboring elements l cannot be arbitrarily decreased. In the designed assembly of seven fiber positioner elements (fiber positioner array) in Fig. 4(a), the distance l is reduced down to $l = 37$ mm.

C. Fiber Collimator Aperture Size and Atmospheric Turbulence Impact

It is well known that atmospheric turbulence causes random displacements of the focal spot centroid (focal spot wander) that are associated with random wavefront tilts of the optical wave entering the lens aperture [13]. For complete precompensation of the turbulence-induced wavefront phase tip and tilt-type aberrations (phase tilts), the fiber tip displacement amplitude Δ should exceed the corresponding range of the focal spot wander. Assuming that the focal spot displacement is only caused by fluctuations of the wavefront angle of arrival at the fiber collimator subaperture, the standard deviation σ_F of the focal spot displacement fluctuations in the weak fluctuation regime can be represented in the form [13], [14]

$$\sigma_F = 0.42f \left(\frac{d}{r_0} \right)^{5/6} \left(\frac{\lambda}{d} \right) \quad (1)$$

where $r_0 = 1.68(C_n^2 k^2 L)^{-3/5}$ is the characteristic Fried parameter for a plane wave propagating in statistically homogeneous and isotropic turbulence over distance L [15]. Here, C_n^2 is the refractive index structure parameter and $k = 2\pi/\lambda$.

The dynamical range of fiber tip displacement Δ should be large enough to provide both full precompensation of wavefront tilts and beamlet pointing at a distant target (conformal beam focusing). For compensation of the turbulence-induced phase tip and tilts with the standard deviation σ_F , the fiber tip displacement Δ should exceed σ_F (by at least twofold). Assuming that an equal fraction of the fiber tip displacement range is designated for the conformal beam focusing, we correspondingly obtain $\Delta = 4\sigma_F$. Substitution of $f = 6d$ and $\sigma_F = 0.25\Delta$ into

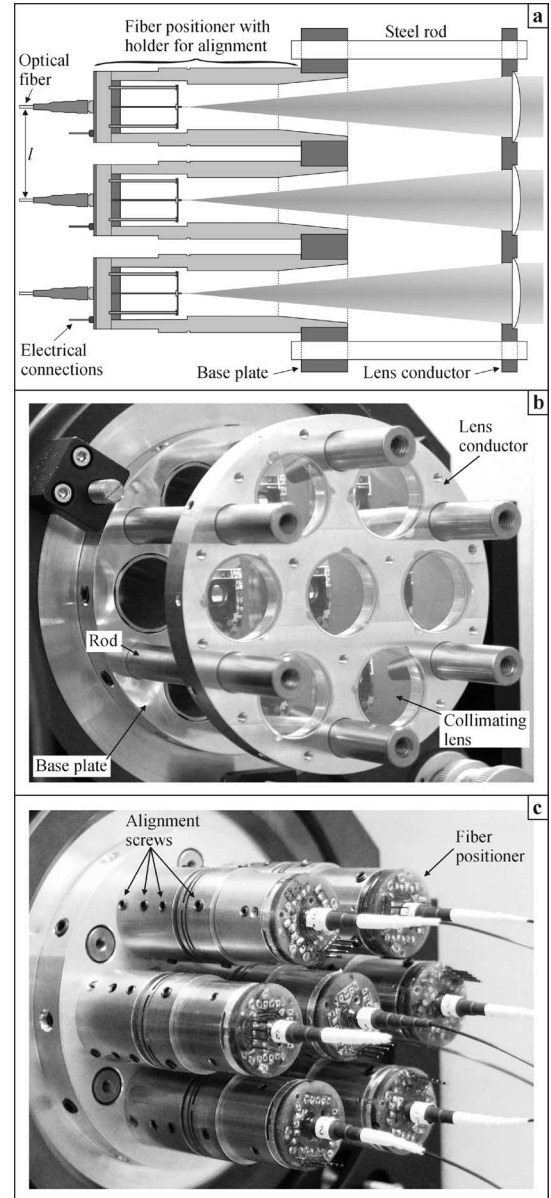


Fig. 4. Fiber collimator array assembly. (a) Schematic of cross section, (b) front side, and (c) backside photographs.

(1) leads to the following estimation:

$$\Delta = 10.08 \left(\frac{d}{r_0} \right)^{5/6} \lambda. \quad (2)$$

For a fixed value of Δ , which is defined by the fiber positioner design, we obtain from (2) the following estimation for the collimating lens diameter:

$$d \leq d_{\text{max}} = 0.06 \left(\frac{\Delta}{\lambda} \right)^{6/5} r_0. \quad (3)$$

For the previously described fiber positioner, from (3), we have $d \leq d_{\text{max}} = 3.55r_0$.

In severe turbulence conditions, the Fried parameter r_0 can be as small as 1.0 cm or even less [16]. Assuming that $r_0 = 1.0$ cm,

we arrive to the following estimation for the collimating lens diameter: $d \leq d_{\max} \approx 36$ mm.

Let us now estimate the residual phase error assuming that both the turbulence-induced piston and tip and tilt aberration components are completely compensated using the array of fiber-integrated phase shifters and fiber tip positioners, respectively. As shown in [17], for the Kolmogorov turbulence model, the mean square residual phase error $\langle \varepsilon_C^2 \rangle$ for the conformal aperture with piston and tip/tilt phase aberration compensation depends only on the phase error at each subaperture and is given by the expression

$$\langle \varepsilon_C^2 \rangle = 0.134 \left(\frac{d}{r_0} \right)^{5/3} \quad (4)$$

where the notation $\langle \rangle$ defines statistical averaging performed over an ensemble of turbulence-induced refractive index fluctuations.

How large can the residual phase error be? Aberrations in optical systems are commonly evaluated using the following inequality known as the Maréchal criterion: $\varepsilon_C = \langle \varepsilon_C^2 \rangle^{1/2} \leq \varepsilon_{th}$, where the phase error threshold value $\varepsilon_{th} \approx \pi/7$ (i.e., approximately equals $\lambda/14$) [18]. The Maréchal criterion corresponds to a Strehl ratio $St > 0.8$, which is defined here as the ratio of the maximum intensity achieved at a remote target with phase aberration precompensation to the corresponding diffraction-limited value [18].

Let us evaluate the residual phase error for a fiber collimator array with subaperture diameter $d = d_{\max}$ using the Maréchal criterion. Substitution of (3) with $d = d_{\max}$ into (4) leads to the following estimation:

$$\langle \varepsilon_C^2 \rangle_{\max} \approx 1.2 \times 10^{-3} \left(\frac{\Delta}{\lambda} \right)^2. \quad (5)$$

For the fiber positioner device described, the residual error obtained based on this formula is unacceptably large: $\varepsilon_C \approx 1.0$ rad.

This residual phase error can be reduced either by using a smaller diameter collimating lens with $d < d_{\max}$ or by incorporating additional AO elements at each fiber array subaperture.

Let us first estimate the fiber collimator aperture diameter $d = d_{pt}$ for which the Maréchal criterion is satisfied with compensation of solely piston and tip and tilt phase distortion components. From (4) with $\langle \varepsilon_C^2 \rangle = \varepsilon_{th}^2$, we have

$$d = d_{pt} \approx 1.28r_0. \quad (6)$$

The obtained subaperture diameter d_{pt} is approximately 2.8-fold smaller than the maximum diameter of the collimating lens that is calculated for the actual range of fiber tip displacement. For comparison, note that in the fiber array system with solely piston-type aberration compensation, the corresponding fiber collimator apertures diameter is $d = d_p \approx 0.38r_0$, i.e., 3.35-fold smaller.

Now consider a fiber array system with precompensation of the first ten Zernike aberrations (including spherical aberration). In this case, the residual error is given by $\langle \varepsilon_C^2 \rangle_{sp} = 0.0377 (d/r_0)^{5/3}$ (see [17] and [19]) and the Maréchal criterion

is satisfied for the fiber collimator apertures with diameter $d = d_{sp} \approx 2.7r_0$. Similar calculations show that compensation of the first 20 Zernike aberrations (including pentafoils) allows a further increase of the subaperture diameter so that $d = d_{pent} \approx 3.9r_0$. From this analysis for $r_0 = 1.0$ cm, we correspondingly obtain $d_{sp} \approx 27$ mm and $d_{pent} \approx 39$ mm. Note that the obtained value d_{pent} only slightly exceeds the maximum subaperture diameter d_{\max} estimated based on the available fiber tip deflection range Δ .

In the fiber array system in Fig. 4, the clear aperture of the collimating lens is $d = 26$ mm. This means that solely piston and tip and tilt aberration precompensation in this fiber array system can be sufficient (in accordance with the Maréchal criterion) for operation in atmospheric turbulence conditions with Fried parameter $r_0 \geq 2$ cm. More severe turbulence conditions require compensation of additional low-order phase aberrations. For example, with precompensation of the first ten low-order Zernike aberrations including spherical aberrations, the Maréchal criterion is fulfilled with a Fried parameter $r_0 \geq 1$ cm.

D. Focal Length of Fiber Collimator Lens and Subaperture Fill Factor

The next important parameter to be considered is the focal distance f of the collimating lens. With the fixed mode field diameter of fiber d_{MFD} and subaperture diameter d , the focal distance f solely defines the radius a_0 of the outgoing collimated Gaussian beam (beamlet), and hence also defines the beamlet divergence and energy losses resulting from the beamlet clipping by the lens aperture. Note that both factors affect intensity distribution and power obtained by focusing the conformal beam onto the target. In the system described, the focal distance f was selected by calculating the outgoing beamlet radius a_0 that maximizes the on-axis intensity I_T^0 obtained by focusing the conformal beam onto the target plane in vacuum [7].

As it is shown in [7], for fiber array systems with $N_{\text{sub}} \geq 7$ and the focusing distance $L \geq 0.01kD^2$, the optimal ratio $f_{\text{sub}} = 2a_0/d$ (subaperture fill factor) is practically independent of the number of subapertures N_{sub} and the focusing distance L , and is approximately equal to $f_{\text{sub}} = 0.89$. Correspondingly, the optimal diameter of the outgoing collimated Gaussian beamlet is $2a_0 = 0.89d \approx 23$ mm. For the measured beam divergence angle from the fiber tip of 78.3 mrad (cone half angle), this beamlet diameter corresponds to the focal distance $f = 147.9$ mm. In the fiber array system described, we used lenses with the focal distance $f = 149$ mm. The subaperture fill factor for these lenses $f_{\text{sub}} = 0.9$ is close to the optimal value.

E. Fiber Array Aperture: Design and Optimization

In the fiber collimator array system described here, the collimating lenses are assembled inside a lens conductor made of an aluminum disk with machined through-holes, as shown in Fig. 4(a) and (b). The lenses are carefully aligned (using an interferometer) to minimize angular deviations in the lens optical axes. Using six steel rods, the lens conductor is attached to the base plate with through-holes. The fiber positioners are installed into special holders that are mounted to the backside of the base plate, as illustrated in Fig. 4(a) and (c). The fiber

positioner holder is designed to provide 6 degrees of freedom for alignment of the fiber tip using a set of alignment screws [see Fig. 4(c)].

In a misaligned fiber array, the fiber tips are displaced from the collimating lens focal points. The fiber tip displacements along the optical axis (in the z -direction) result in generation of beamlets that have slightly different divergence, while fiber tip displacements in the orthogonal plane (in the x - y direction) lead to deviations in the beamlet propagation angles.

Besides the x - y - z displacement, the fiber tip cleaved surface can be tilted with respect to the plane orthogonal to the optical axis resulting in an offset between the centers of the collimating lens and the beamlet at the lens pupil plane. Compensation of the offsets due to nonorthogonal fiber tip cleave angles is achieved using angular alignment of the fiber tips. Thus, the fiber array aperture requires careful alignment of all seven fiber tips inside the fiber positioner holders as well as an alignment of the beamlet polarization states (by rotating the fiber positioner holders inside the base plate).

An example of the intensity pattern emitted by the fiber array aperture is shown in Fig. 5(a). Note that although the beamlets are accurately centered, the outgoing beamlet power varies from one subaperture to another, which can be explained by unequal power losses in the fiber channels. This variation in the output power between subapertures has both steady state and relatively slow varying components. Equalization of optical power at the system subapertures was achieved using feedback control of the array of intensity modulators of the multichannel fiber system (see Section III-D). The results of power equalization are illustrated in Fig. 5(b) and (c).

In the design of the fiber array, we paid special attention to optimization of the conformal aperture fill factor $f_C = l/d$ by reducing the distance l between the centers of neighboring subapertures. The decrease of the ratio $f_C = l/d$ is highly desired as it sharply decreases the amount of energy concentrated in the side lobes of the focused conformal beam [7].

Besides the decrease in f_C , reducing the distance l between the neighboring subapertures, permits wider range of the conformal beam focusing. Indeed, it is easy to show that the minimal focusing distance L_{\min} is defined by the condition $L_{\min} = l(f/\Delta)$, i.e., the distance L_{\min} is proportional to the distance l between subapertures, the focal length of the collimating lens f , and inversely proportional to the fiber tip displacement amplitude Δ . In the fiber array described, $f_C = 1.42$ and $L_{\min} = 184$ m. By taking into account that only half of the fiber tip displacement range Δ was assigned for the conformal beam focusing, the expected minimal distance $L_{\min} = 368$ m.

III. FEEDBACK CONTROL IN ADAPTIVE ARRAY OF FIBER COLLIMATORS

A. Experimental Setup

Performance of the adaptive fiber collimator array with both piston and tip and tilt feedback control was analyzed using the experimental setup shown in Fig. 6. The conformal laser beam that is composed of seven collimated beamlets at the fiber collimator array pupil was focused by the lens L_1 with the focal

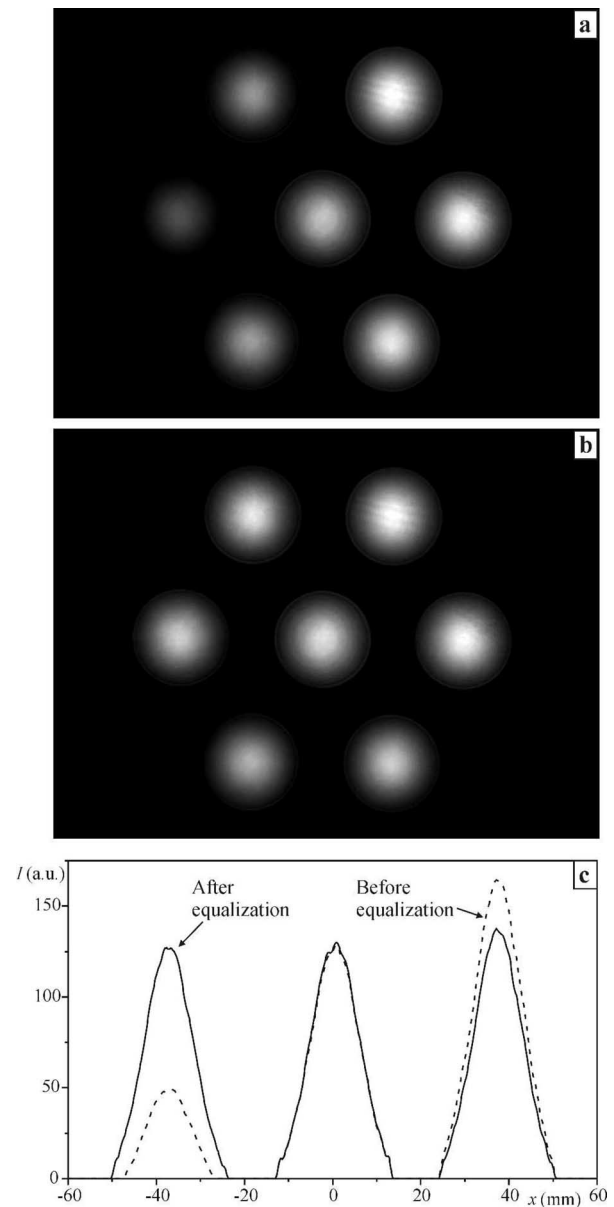


Fig. 5. Intensity distribution patterns (a) and (b), and the corresponding cross-section intensity profiles (c) in the fiber collimator array pupil plane before (a) and after (b) equalization of power within subapertures by means of control of fiber-based intensity modulators.

distance $F = 1.9$ m onto a pinhole located in the lens focal plane. The folding mirrors M_1 and M_2 in Fig. 6 were used for alignment purposes. The pinhole diameter b_{ph} of $20 \mu\text{m}$ is smaller than the diameter of the Airy disk $b_{Airy}^D = 49 \mu\text{m}$ for the conformal beam aperture of diameter $D = 100 \mu\text{m}$. The corresponding Airy disk diameter for a single beamlet is $b_{Airy}^d = 190 \mu\text{m}$.

A single-pixel photodetector with 0.5 mm diameter was used to measure the optical power that passed through the pinhole. The photodetector was located approximately 2 mm behind the pinhole. The output signal (voltage) of the photodetector J_{PIB} , referred to here as the power-in-the-bucket metric, was sent to three different controllers driving the seven phase shifters and intensity modulators of the multichannel fiber system

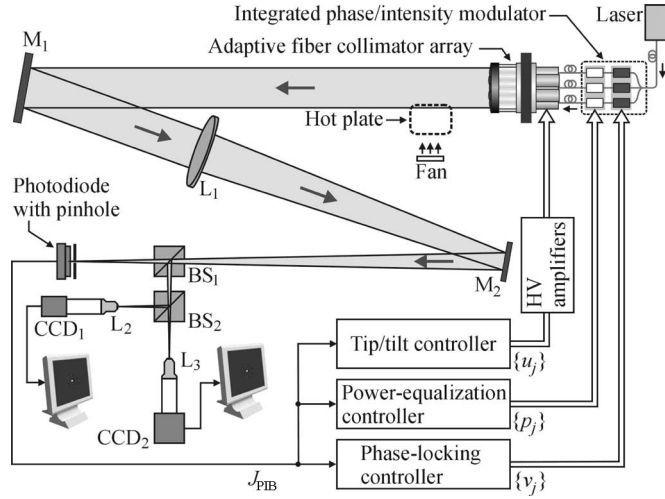


Fig. 6. Schematics of the experimental setup for performance evaluation of the adaptive fiber collimator array.

(phase-locking and power equalizing controllers), and seven fiber positioners (tip-tilt controller). All three feedback control systems with the total number of control channels 28 are based on the stochastic parallel gradient descent (SPGD) optimization algorithm configured for metric J_{PIB} maximization (see Section III-B) [20]–[22].

Using two beam splitters (BS_1 and BS_2) and microscope objective lenses (L_2 and L_3), as shown in Fig. 6, the focal spot of the conformal beam was reimaged onto the charge-coupled device (CCD) cameras CCD_1 and CCD_2 . This reimaging was performed with different focal spot magnification to provide both wide and narrow field of view (FOV) images of the lens L_1 focal plane.

The wide FOV imaging system was intended for the coarse alignment of beamlets using the alignment screws, as shown in Fig. 4(c). The narrow FOV images of the conformal beam focal plane intensity distribution were obtained using a high-resolution CCD with 1024×1024 pixels, 12-bit gray-scale resolution, and a fill factor of 100%. The imaging data (movies) obtained with this camera were used as an independent information source for adaptive system performance evaluation.

B. Control System Architecture and Algorithms

The control system of the fiber collimator array consisted of the following three controllers: 1) a specialized fast SPGD phase-locking controller for driving arrays of seven LiNbO_3 -based phase shifters; 2) a PC-based SPGD controller used for equalization of the beamlet power levels by driving an array of seven intensity modulators (waveguide-integrated Mach-Zehnder interferometers); and 3) a PC-based SPGD controller driving seven fiber positioners for precompensation of wavefront phase tip and tilt aberration at each subaperture (SPGD tip-tilt controller).

In all three controllers, the control voltage update was performed using the following SPGD iterative algorithm [22]–[24]:

$$a_j^{(n+1)} = a_j^{(n)} + \gamma^{(n)} \delta a_j^{(n)} \delta J_{\text{PIB}}^{(n)}, \quad j = 1, \dots, N, \quad n = 1, \dots \quad (7)$$

where $a_j^{(n)}$ is the control voltage (control) at the n th iteration, which is applied to the j electrode of either the phase shifter array (in this case $a_j^{(n)} \equiv v_j^{(n)}$, $j = 1, \dots, 7$), or the intensity-modulator array (in this case $a_j^{(n)} \equiv p_j^{(n)}$, $j = 1, \dots, 7$), or the fiber tip positioners (in this case $a_j^{(n)} \equiv u_j^{(n)}$, $j = 1, \dots, 14$). Note that one fiber positioner requires two control channels for providing displacement of the fiber tip in x - and y -direction, as discussed in Section II-B.

In (7), $\delta a_j^{(n)} = \kappa^{(n)} \delta p_j^{(n)}$ is a small amplitude voltage perturbation (typically 3%–5% of the control signal full dynamical range) applied to the j th electrode at the n th iteration, $\kappa^{(n)}$ is the perturbation amplitude, $\gamma^{(n)}$ is the gain coefficient, and $\delta J_{\text{PIB}}^{(n)}$ is the metric perturbation. In the expression for the perturbation, $\{\delta p_j^{(n)}\}$ are a precalculated set of random numbers with zero mean and a predefined probability distribution. In most cases, we used either the Bernoulli (coin-type) probability distribution or a probability distribution corresponding to an approximation of Kolmogorov phase screen realizations using piston and tip and tilt aberration coefficients [18]. For each of the SPGD control systems, the perturbations were simultaneously applied to all electrodes of the control system and used to calculate the corresponding metric perturbation $\delta J_{\text{PIB}}^{(n)}$.

The gain coefficient $\gamma^{(n)}$ in (7) and the perturbation amplitude $\kappa^{(n)}$ were functions of the current metric value [22], [24], [25]

$$\gamma^{(n)} = \gamma_0 \left(\frac{J_{\text{opt}}}{J_{\text{opt}} + J^{(n)}} \right)^p, \quad \kappa^{(n)} = \kappa_0 \left(\frac{J_{\text{opt}}}{J_{\text{opt}} + J^{(n)}} \right)^q \quad (8)$$

where J_{opt} is an expected maximum metric value, γ_0 and κ_0 are gain and perturbation amplitude coefficients, and p and q control the rate of change of the functions. The parameters p , q , γ_0 , and κ_0 in (8) were selected separately for each control system used.

All three SPGD control systems operated asynchronously using the same metric signal (asynchronous SPGD control [26]) but with significantly different iteration rates. The maximum iteration rate for the phase-locking SPGD controller was approximately 180 000 iterations per second. The iteration rate of the tip-tilt SPGD control system was approximately 3000 iterations per second. The third SPGD feedback control system was operating at approximately 50 iterations per second. This system was used for equalization of the relatively slow changing power levels of the fiber collimators beamlets.

C. Phase-Locking SPGD Controller

To achieve the fastest iteration rate, the phase-locking control system was based on a microprocessor (AT91SAM9260). Although the system can operate with 180 000 SPGD iterations per second in the experiments described, we used the iteration rate of 100 000 iterations per second, which provided higher signal-to-noise ratio in metric measurements and more stable adaptation process convergence.

The dynamical range of the output voltages applied to the phase shifters (± 25 V) corresponded to the phase shift range of approximately $\pm 10\pi$ rad. The controller performed subtraction (if this was necessary) of the predefined voltage values $\{u_j^{\text{res}}\}$

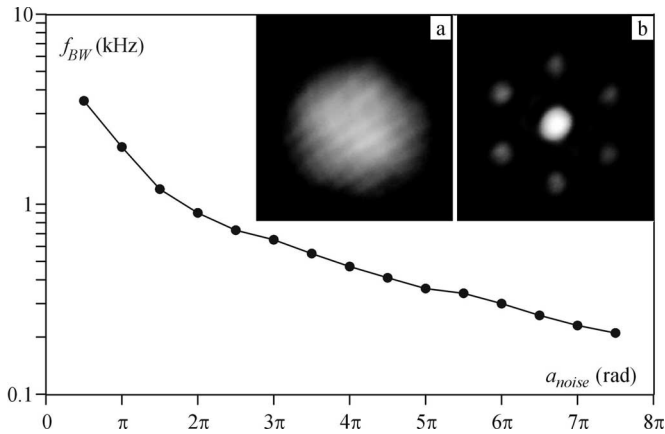


Fig. 7. Closed-loop bandwidth frequency f_{BW} of the phase-locking controller as a function the phase noise amplitude a_{noise} . The insets show long-exposure focal plane images of the conformal beam with the phase-locking controller (a) OFF and (b) ON.

(reset voltages) to keep control voltages inside the reset ranges of $[-v_j^{res}, v_j^{res}]$. These reset ranges correspond to $\pm 2\pi n_{res}$ phase shifts, where $1 \leq n_{res} \leq 5$ is a predefined integer number. The reset voltages $\{v_j^{res}\}$ were carefully measured and used as a lookup table for the phase-locking microprocessor system. Implementation of 2π -reset operation significantly improved phase-locking control system stability and phase-locking accuracy.

To evaluate phase-locking controller closed-loop bandwidth, the multichannel fiber system was modified to include an additional array of seven phase shifters. These phase shifters (identical to the phase shifters of phase-locking system) were used to inject a piston-type phase aberration (phase noise) in the form of the sine signals $\{a_{noise} \sin(2\pi f_j t)\}$, where a_{noise} is the phase noise amplitude and $\{f_j\}$ are a set of different frequencies. The performance of the phase-locking system was estimated using the measured ratio $\eta_{PL} = \langle J_{PIB} \rangle / \langle J_{PIB}^0 \rangle$ of the power-in-the-bucket metric time-averaged value $\langle J_{PIB} \rangle$ obtained for the phase-locking system operation in the presence of phase noise to the corresponding metric value $\langle J_{PIB}^0 \rangle$ measured with the phase noise amplitude set equal to zero. The ratio η_{PL} is a function of both the noise amplitude a_{noise} and the frequencies $\{f_j\}$. To decrease the number of parameters, the frequencies $\{f_j\}$ were chosen in the form $f_j = f_{max}(1 - 0.1j)$, where $j = 1, \dots, 7$. In this case, the performance metric η_{PL} is a function of two parameters: $\eta_{PL} = \eta_{PL}(a_{noise}, f_{max})$.

The phase-locking control system closed-loop bandwidth frequency f_{BW} was defined from the condition $\eta_{PL}(a_{noise}, f_{BW}) = 0.5$, which corresponds to 3 dB compensation efficiency drop. The dependence of the measured closed-loop bandwidth frequency f_{BW} on the phase noise amplitude a_{noise} is shown in Fig. 7. As seen from this dependence, the closed-loop bandwidth frequency decreases with the increase of the phase noise amplitude. The results suggest that, for the current implementation of the phase-locking controller with operational speed of 100 000 iteration per second, severe uncorrelated piston-type phase aberrations with an amplitude of 1.5π rad can be efficiently compensated with a closed-loop bandwidth frequency exceeding 1.0 kHz. The current electronic sys-

tem can be further improved to nearly double operational speed and achieve >1.0 kHz closed-loop bandwidth for compensation of piston-type aberrations within an amplitude range of 2π rad. The photographs in Fig. 7 illustrate the phase-locking control system operation in the presence of phase noise. The focal plane intensity distribution patterns (conformal beam focal spot) are shown without [Fig. 7(a)] and with [Fig. 7(b)] phase-locking feedback control.

D. Tip-Tilt Control System

The SPGD tip-tilt control system was implemented using a 3.2-GHz PC equipped with analog input and output cards. A set of 14 high-voltage amplifiers was used to amplify control signals $\{u_j(t)\}$, ($j = 1, \dots, 14$) to the range $[-70 \text{ V}, 70 \text{ V}]$. The amplified control voltages were applied to the electrodes of the fiber positioners resulting in x and y displacements of the fiber tips in the fiber collimators. Although the maximum operational speed that can be achieved with the PC controller was approximately 10 000 SPGD iterations per second, the iteration rate was reduced down to 5000 iterations per second to maintain stable operation of the feedback control loop in wide range of parameters p , q , γ_0 , and κ_0 in (8). With the increase of the iteration rate, the range of the SPGD control parameters corresponding to the stable system operation got smaller due to presence of high-order mechanical resonances of the fiber positioners.

The characteristic convergence time τ_{tilt} of tip and tilt phase aberration compensation (also referred to as the tip-tilt control system response time) was estimated using the following procedure. With the phase-locking control loop closed, a set of random voltages $\{u_j(0)\}$ with the uniform probability distribution inside the range $[-u_0, u_0]$ was applied to all 14 electrodes of the fiber positioners resulting in random wavefront phase tilts of the outgoing beamlets and decrease of the power-in-the-bucket metric value J_{PIB} . At this starting condition, the tip-tilt control system was switched on and operated during time T (~ 2 s) long enough to ensure convergence of the transition process of the metric J_{PIB} . The dependences of $J_{PIB}(t)$ were measured for a large (>50) set of random initial conditions $\{u_j(0)\}$ belonging to a fixed range $[-u_0, u_0]$, and the results were averaged. The obtained averaged convergence characteristic $\langle J_{PIB}(t) \rangle$ was used for the estimation of the characteristic convergence time τ_{tilt} , which was defined as the time required for recovery of 80% of the optimum metric value and was calculated based on the following equation: $\langle J_{PIB}(\tau_{tilt}) \rangle = 0.8 \langle J_{PIB}(T) \rangle$. The measurements of τ_{tilt} performed for different amplitudes u_0 showed monotonic increase of the convergence time τ_{tilt} with increase of u_0 . For example, for the range of initial conditions with $u_0 \approx 10$ V and the corresponding misalignment of the outgoing beamlets within angular range of $\theta_0 \leq 50 \mu\text{rad}$, the measured convergence time was $\tau_{tilt} \approx 30$ ms, while for $u_0 \approx 30$ V, it increased up to $\tau_{tilt} \approx 150$ ms. In addition, the increase of u_0 above approximately 30 V resulted in a sharp decrease of the achieved metric value $\langle J_{PIB}(T) \rangle$, which indicates only partial compensation of the induced misalignments.

For large amplitude angular misalignment, the focal spot of the corresponding beamlet may not overlap with the other

beamlets during the entire adaptation process. This severely misaligned beamlet does not contribute to the coherent combining (interference) of the focal spots originating from the less misaligned beamlets. This results in appearance of a local extremum in the dependence of the metric J_{PIB} on the control variables (voltages), an overall decrease of the achieved metric value $\langle J_{\text{PIB}}(T) \rangle$, and a slow down of the adaptation convergence process.

E. Power Equalization Control System

In the course of experiments with the adaptive fiber collimator array, we observed slow variations not only of the total power emitted by the fiber collimator array but also the relative powers at the output of each fiber collimator. These changes typically were on the order of 10%–15% and occurred on a time scale of 0.5–10 s. It seems that the major factor causing these changes is related with drifts of the phase differences in the integrated intensity controller array (Mach–Zehnder interferometers). Since each set of experiments with phase-locking and tip and tilts aberration compensation typically lasted several minutes, these changes in the beamlet relative powers were highly undesired.

For equalization of the beamlet power levels, we used a slower operating PC-based SPGD controller with an architecture similar to the tip-tilt controller. Utilizing the same power-in-the-bucket metric optimization, the power equalization controller supplied voltages to seven electrodes of the fiber-integrated intensity modulator. The experiments show that with active power stabilization, the fluctuations in power of the outgoing beamlets were reduced to less than 1.5%. Note that in the experiments described in the following section, the power equalization control system was always on.

IV. COMPENSATION OF DYNAMICAL PHASE DISTORTIONS WITH ADAPTIVE FIBER COLLIMATOR ARRAY

A. Laboratory-Generated Dynamical Phase Aberrations

The high adaptation rates achieved in the phase-locking and tip-tilt SPGD control systems allowed us to perform experiments with compensation of dynamical phase aberrations originating from an electrical heater and fan-induced turbulent flows. The goal of these experiments was to analyze the efficiency of adaptive precompensation of wavefront phase piston and tilt-type phase aberration components in the fiber collimator array system.

In the experimental setup shown in Fig. 6, the electric heater (hot plate) was located approximately 20 cm below the conformal beam with 10 cm offset from the optical axis. The air flow was created by a small fan located behind the hot plate. The air flow was directed toward the fiber collimator array orthogonal to the beam propagation direction. The mutual positions of conformal laser beam, heater, and fan are shown in Fig. 6.

The turbulence strength was controlled by changing the temperature of the hot plate surface by sequentially switching the knob between position 0 (power off) and position 6 corresponding to approximately 180 °C at the hot plate surface. Thus, the position of the knob of the hot plate can be associated with

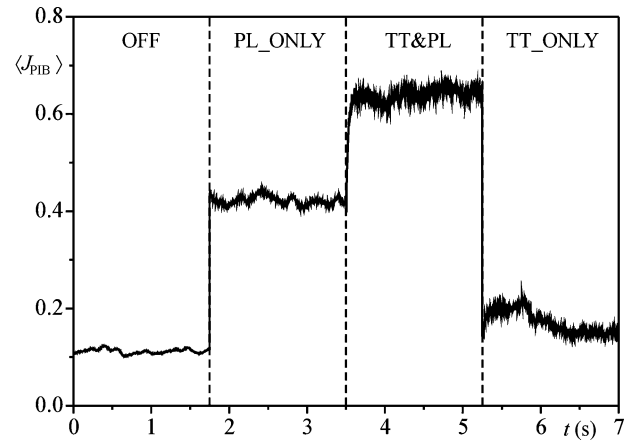


Fig. 8. Averaged evolution curve $\langle J_{\text{PIB}}(t) \rangle$ of the power-in-the-bucket metric for adaptation trials with four different operation phases: OFF—both phase-locking and tip-tilt controllers are OFF, PL_ONLY—only the phase-locking controller is ON, TT&PL—both tip-tilt and phase-locking controllers are ON, and TT_ONLY—only tip-tilt control is ON.

turbulence strength and correspondingly referred to here as turbulence 1 (knob in the first position) through turbulence 6 (knob in the position 6) for convenience.

B. Adaptation Trials

Performance of dynamic phase distortion compensation was estimated using the following procedure referred to here as an *adaptation trial*. Each adaptation trial lasted approximately 7 s and included the following four sequential phases.

- 1) *OFF*: During this phase, both phase-locking and tip-tilt SPGD controllers were OFF and the voltages on both the phase shifters and fiber positioners were fixed. These control voltages are referred to as initial conditions.
- 2) *PL_ONLY*: In this phase, only the phase-locking control loop was closed while the control voltages on the fiber positioners were fixed.
- 3) *PL&TT*: During this phase, both the phase-locking and tip-tilt SPGD controllers were ON.
- 4) *TT_ONLY*: In this phase, only the tip-tilt SPGD controller was operating and the voltages on phase shifters were fixed.

During the adaptation trial, the metric values $J_{\text{PIB}}(m)$ ($m = 1, \dots, M$) were recorded at a rate of ~ 5 kHz that allowed us to obtain the temporal behavior of the optimized metric $J_{\text{PIB}}(t)$. Continuous changes in the turbulent flow resulted in variations in the adaptation trials. In order to decrease dependence of the compensation performance on randomly varying conditions, a large number (typically 100) of sequential adaptation trials were recorded and averaged.

C. AO Compensation Results

An example of the averaged time-evolution dependence $\langle J_{\text{PIB}}(t) \rangle$ obtained for the turbulence 4 is shown in Fig. 8. The averaged metric curve shows significant improvement achieved by compensation of piston-type aberrations with the SPGD phase-locking control system (see the transition between phases OFF and PL_ONLY). Also note the fast convergence

of the adaptation process after the phase-locking system was switched on. Additional precompensation of wavefront tip and tilt aberrations with the tip-tilt control system resulted in further increase of the optimized metric (see the transition between phases PL_ONLY and PL&TT), although the performance improvement was somewhat less and achieved during a longer convergence time if compared to phase-locking control. Note that at the beginning of each adaptation phase, we used as the initial conditions the set of control voltages obtained by averaging of control voltages in each channel that were obtained during the PL&TT phase in the previous adaptation trial.

As seen from the averaged adaptation curve in Fig. 8, precompensation of tip and tilt aberrations at each subaperture resulted in only relatively small metric improvement when the phase-locking system was OFF (see transition between phase TT_ONLY and OFF).

During the adaptation trials, we computed metric histograms corresponding to each of the four operational phases. Averaged over the large number of adaptation trials and normalized, these histograms characterize the probability distribution $p(J_{PIB})$ of metric values. The metric histograms obtained by averaging a set of 100 adaptation trials for different turbulence conditions are presented in Fig. 9.

Each plot in Fig. 9 shows four histograms corresponding to the adaptation phases described earlier. The histogram width characterizes the metric fluctuation level, while the position of the histogram curve center of mass (first moment) corresponds to the averaged metric value. The histogram curves thus characterize both the averaged metric value and metric fluctuation level achieved with adaptive control.

Consider first the metric histograms obtained in absence of turbulence [Fig. 9(a)]. The OFF histogram (all control systems are OFF) is quite wide and bumpy. This indicates that the conformal beam focal plane spot was unstable. This instability is related with time-varying random phase shifts originating in the fiber system. The inset photograph A in Fig. 9(a) shows typical focal plane intensity patterns with the phase-locking control system OFF. The histogram obtained with the closed-loop tip-tilt control (TT histogram) is noticeably shifted toward bigger metric values, but is still widely spread, which indicates a relatively high level of metric fluctuations.

The histogram obtained with the operating phase-locking control system (PL histogram) is further shifted to the range of bigger metric values. Nevertheless, the most noticeable change occurred with the histogram shape. The PL histogram is significantly narrower—an indication that phase-locking resulted in a stable focal plane pattern, as shown in Fig. 9(a) (inset photograph B). Additional compensation of wavefront tip and tilt aberrations (PL&TT histogram) resulted in a small shift of the histogram toward smaller metric values that indicates a small (<3%) decrease of the averaged metric value. This effect can be explained by presence of the tip-tilt-control-system-induced perturbations resulting in average metric decrease. In absence of turbulence, precompensation of wavefront tilts is not required.

Now consider the moderate turbulence regime in Fig. 9(b) (turbulence strength 3). In this case, the TT histogram maximum is shifted with respect to the OFF histogram toward bigger met-

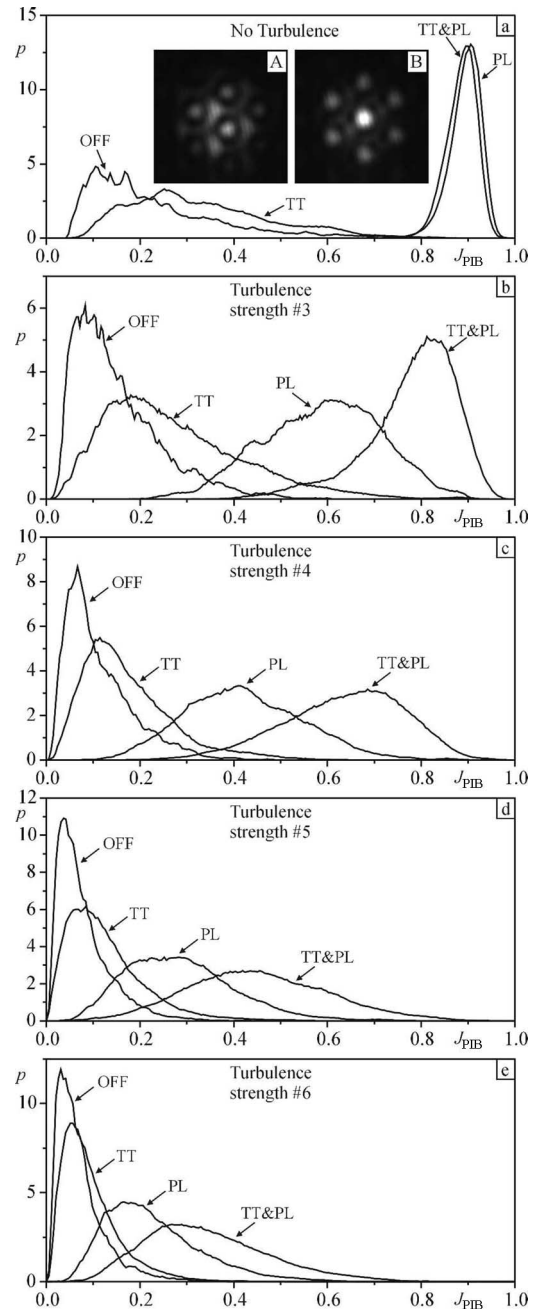


Fig. 9. Histograms (probability density distributions p) for metric values J_{PIB} obtained under different turbulence conditions. (a) No turbulence. (b)–(e) With turbulence. Labels on the curves correspond to OFF—all feedback controllers are OFF, TT—only tip-tilt controller is ON, PL—only phase-locking controller is ON, and TT&PL—both tip-tilt and phase-locking controllers are ON. Gray-scale images in (a) correspond to focal plane intensity distributions without (A) and with (B) phase-locking control ON.

ric values, which indicates that tip-tilt control only resulted in the increase of the averaged metric value. Nevertheless, the metric fluctuations in this regime are quite high and the TT histogram is correspondingly wide. As the PL histogram in Fig. 9(b) shows, phase-locking control leads to significant performance improvement (higher averaged metric value and smaller fluctuations). Additional precompensation of tip and tilt aberrations in the phase-locked system results in a considerable performance

improvement [see PL&TT curve in Fig. 9(b)], which is relatively close to the performance in absence of turbulence.

In the cases of the turbulence strength 4, the difference between no compensation and piston (phase-locking) plus additional wavefront tip and tilt aberration precompensation is the most distinguished. This case illustrates adaptive compensation in the turbulence conditions for which incorporation of tip and tilt compensation capabilities into the fiber collimator array gives the most significant performance improvement.

With the further increase of turbulence strength shown in Fig. 9(d) and (e), both OFF and TT histograms are rather close to each other. This means that the turbulence is so strong that tip-tilt compensation is not efficient. Also, PL and PL&TT histograms are closer to the OFF curve, although even for the strongest turbulence case [Fig. 9(e)], an about four times metric improvement was achieved with simultaneous phase-locking and tip-tilt control when compared to the uncompensated case.

ACKNOWLEDGMENT

The authors are grateful to J. Mangano for his continuous interest, encouragement, and many fruitful discussions. They also thank P. McManamon for technical comments and S. Lachinova for help in theoretical analyses. This research and development was performed at the U.S. Army Research Laboratory's (ARL) Intelligent Optics Laboratory, Adelphi, MD.

REFERENCES

- [1] M. Minden, "Coherent coupling of a fiber amplifier array," in *13th Annu. Solid State Diode Laser Technol. Rev. (SSDLTR) 2000 Tech. Dig.*, Air Force Research Lab, pp. 1–15.
- [2] H. Bruesselbach, S. Wang, M. Minden, D. C. Jones, and M. Mangir, "Power-scalable phase-compensating fiber-array transceiver for laser communications through the atmosphere," *J. Opt. Soc. Amer. B*, vol. 22, no. 2, pp. 347–353, Feb. 2005.
- [3] S. J. Augst, J. K. Ranka, T. Y. Fan, and A. Sanchez, "Beam combining of ytterbium fiber amplifiers," *J. Opt. Soc. Amer. B*, vol. 24, no. 8, pp. 1707–1715, Aug. 2007.
- [4] T. M. Shay, V. Benham, J. T. Baker, B. Warda, A. D. Sanchez, M. A. Culpepper, D. Pilkington, J. Spring, D. J. Nelson, and C. A. Lua, "First experimental demonstration of self synchronous phase locking of an optical array," *Opt. Exp.*, vol. 14, no. 25, pp. 12015–12021, Dec. 2006.
- [5] P. McManamon and W. Thompson, "Phased array of phased arrays (PAPA) laser systems architecture," *Fiber Integr. Opt.*, vol. 22, no. 2, pp. 79–88, Mar./Apr. 2003.
- [6] J. E. Kinsky, C. X. Yu, D. V. Murphy, S. E. J. Shaw, R. C. Lawrence, and C. Higgs, "Beam control of a 2D polarization maintaining fiber optic phased array with high-fiber count," *Proc. SPIE*, vol. 6306, pp. 63060G-1–63060G-11, 2006.
- [7] M. A. Vorontsov and S. L. Lachinova, "Laser beam projection with adaptive array of fiber collimators. I. Basic consideration for analysis," *J. Opt. Soc. Amer. A*, vol. 25, no. 8, pp. 1949–1959, Aug. 2008.
- [8] M. A. Vorontsov, "Decoupled stochastic parallel gradient descent optimization for adaptive optics: Integrated approach for wave-front sensor information fusion," *J. Opt. Soc. Amer. A*, vol. 19, no. 2, pp. 356–368, Feb. 2002.
- [9] (2007). [Online]. Available: www.eospace.com
- [10] L. A. Beresnev and M. A. Vorontsov, "Compact fiber bimorph positioner with wide frequency bandwidth," Patent Disclosure, Army Research Lab., Adelphi, MD, Oct. 30, 2007.
- [11] L. A. Beresnev and M. A. Vorontsov, "Design of adaptive fiber optics collimator for free-space communication laser transceiver," *Proc. SPIE*, vol. 5895, pp. 58950R-1–58950R-7, 2005.
- [12] L. A. Beresnev, T. Weyrauch, M. A. Vorontsov, L. Liu, and G. W. Carhart, "Development of adaptive fiber collimators for conformal fiber-based beam projection systems," *Proc. SPIE*, vol. 7090, pp. 709008-1–709008-10, 2008.
- [13] V. I. Tatarskii, *Wave Propagation in a Turbulent Medium*. New York: McGraw-Hill, 1961.
- [14] M. Vorontsov and A. Kohnle, "Optical waves in atmospheric turbulence," FGAN-FOM, Ettlingen, Germany, Rep. FOM 2005/17, Dec. 8, 2005.
- [15] D. L. Fried, "Optical resolution through a randomly, inhomogeneous medium for very long and very short, exposures," *J. Opt. Soc. Amer.*, vol. 56, no. 10, pp. 1372–1379, Oct. 1966.
- [16] A. Tunick, "Optical turbulence parameters characterized via optical measurements over a 2.33 km free-space laser path," *Opt. Exp.*, vol. 16, no. 19, pp. 14645–14654, Sep. 2008.
- [17] S. L. Lachinova and M. A. Vorontsov, "Laser beam projection with adaptive array of fiber collimators. II. Analysis of atmospheric compensation efficiency," *J. Opt. Soc. Amer. A*, vol. 25, no. 8, pp. 1960–1973, Aug. 2008.
- [18] J. W. Hardy, *Adaptive Optics for Astronomical Telescopes*. New York: Oxford Univ. Press, 1998.
- [19] R. J. Noll, "Zernike polynomials and atmospheric turbulence," *J. Opt. Soc. Amer.*, vol. 66, no. 3, pp. 207–211, Mar. 1976.
- [20] M. A. Vorontsov, G. W. Carhart, and J. C. Ricklin, "Adaptive phase-distortion correction based on parallel gradient-descent optimization," *Opt. Lett.*, vol. 22, no. 12, pp. 907–909, Jun. 1997.
- [21] M. A. Vorontsov and V. P. Sivokon, "Stochastic parallel-gradient-descent technique for high-resolution wave-front phase-distortion correction," *J. Opt. Soc. Amer. A*, vol. 15, no. 10, pp. 2745–2758, Oct. 1998.
- [22] M. Vorontsov, J. Riker, G. Carhart, V. S. Rao Gudimetla, L. Beresnev, T. Weyrauch, and L. Roberts, "Deep turbulence effects compensation experiments with a cascaded adaptive optics system using a 3.63 m telescope," *Appl. Opt.*, vol. 48, no. 1, pp. 47–57, Jan. 2009.
- [23] M. A. Vorontsov, G. W. Carhart, M. Cohen, and G. Cauwenberghs, "Adaptive optics based on analog parallel stochastic optimization: Analysis and experimental demonstration," *J. Opt. Soc. Amer. A*, vol. 17, no. 8, pp. 1440–1453, Aug. 2000.
- [24] T. Weyrauch and M. A. Vorontsov, "Atmospheric compensation with a speckle beacon under strong scintillation conditions: Directed energy and laser communication applications," *Appl. Opt.*, vol. 44, no. 30, pp. 6388–6401, Oct. 2005.
- [25] T. Weyrauch, M. A. Vorontsov, T. G. Bifano, J. Hammer, M. Cohen, and G. Cauwenberghs, "Micro-scale adaptive optics: Wavefront control with a μ -mirror array and a VLSI stochastic gradient descent controller," *Appl. Opt.*, vol. 40, no. 24, pp. 4243–4253, Aug. 2001.
- [26] M. A. Vorontsov and G. W. Carhart, "Adaptive wavefront control with asynchronous stochastic parallel gradient descent clusters," *J. Opt. Soc. Amer. A*, vol. 23, no. 10, pp. 2613–2622, Oct. 2006.

Mikhail A. Vorontsov received the Ph.D. degree in physics and the Dr.Sci. degree in physics and mathematics from Moscow State University, Moscow, Russia, in 1977 and 1989, respectively.

He is currently a Senior Physicist in the Computational and Information Sciences Directorate, U.S. Army Research Laboratory, Adelphi, MD, and also a faculty member at the University of Maryland, College Park.

Dr. Vorontsov is a Fellow of the Army Research Laboratory (ARL), the International Society for Optical Engineers (SPIE), and the Optical Society of America (OSA).

Thomas Weyrauch received the Diplom-Physiker degree and the Ph.D. (Dr. rer. nat.) degree in physics from the Technische Universität Darmstadt (TUD), Darmstadt, Germany, in 1990 and 1997, respectively.

He is currently an Assistant Research Scientist at the Institute for Systems Research, University of Maryland, College Park. He was a National Research Council (NRC) Research Associate at the U.S. Army Research Laboratory, Adelphi, MD (2000–2003), a Visiting Scientist at New Mexico State University's Klipsch School of Electrical and Computer Engineering (1999–2000), and a Research Associate at the Institute of Physical Chemistry, Technische Universität Darmstadt (1991–1999).

Dr. Weyrauch is a member of the International Society for Optical Engineers (SPIE), the Optical Society of America (OSA), and the German Physical Society (DPG).

Leonid A. Beresnev received the Ph.D. degree in physics and mathematics from the Solid State Physics Institute, Russian Academy of Sciences (RAS), Moscow, Russia, in 1979.

He was with the chemical industry of Russia and the Institute of Crystallography, RAS, where he was engaged in research and development of thin solid films and liquid crystals. He is currently a Physicist in the Computational and Information Sciences Directorate, U.S. Army Research Laboratory, Adelphi, MD.

Gary W. Carhart was with the University of New Mexico and New Mexico State University studying astronomy, physics, computer science, electrical engineering, and optics. He was with the Air Force Weapons Laboratory as a Computer Engineer trainee, System Industries, Inc., as a Field Service Engineer, and the New Mexico State University as a Research Assistant and Systems Technologist. He is currently a Computer Scientist in the Computational and Information Sciences Directorate, U.S. Army Research Laboratory, Adelphi, MD. His current research interests include adaptive optics, imaging through turbulence, synthetic image fusion, and adaptive laser communication.

Ling Liu received the B.S. degree in mechanical engineering and the M.S. degree in nuclear energy engineering in 1997 and 2000, respectively, from Tsinghua University, Beijing, China, the M.Eng. degree and the M.S. degree in electrical and computer engineering in 2002 and 2008, respectively, from the University of Maryland (UMD), College Park, and the Ph.D. degree in electrical engineering from the UMD, in September 2008.

He is currently a Graduate Research Assistant in the Intelligent Optics Laboratory, Institute for Systems Research, UMD. His current research interests include adaptive optics, adaptive phase-locked fiber arrays, and related control system implementations.

Konley Aschenbach received the B.Sc. degree in computer science from the University of Maryland, College Park, in 2004.

He is currently a Computer Scientist at the U.S. Army Research Laboratory developing software for adaptive optics.